Autonomous Take-Off and Landing of a Low Cost Unmanned Aerial Vehicle

***Jan-Cor Roos*[a] *and Iain K. Peddle*[b]**

Received 10 December 2008, in revised form 15 July 2009 and accepted 7 September 2009

This paper presents the development and results of initial research conducted by Stellenbosch University's Centre of Expertise in Autonomous Systems on autonomous take-off and landing (ATOL) algorithms for a fixed wing unmanned aerial vehicle (UAV). A proposed breakdown of the various phases involved in the take-off and landing sequences is presented, with specific focus on low cost automation solutions. With the phases identified, the ATOL problem is reduced to that of guiding the aircraft from one phase to the next. To this end, classes of controllers that enable the successful execution of the phases are identified and their designs discussed. An aircraft model for simulation and control system design purposes is also presented with specific focus on the runway model. Hardware in the loop simulation results verify the theoretical functionality of the ATOL control algorithms. Flight test results demonstrate the practical success of the ATOL system.

Nomenclature

Roman

C_D	Aerodynamic drag coefficient
C_L	Aerodynamic lift coefficient
C_α	Cornering stiffness
$C_{\alpha\alpha}$	Cornering coefficient
E	East displacement
F	Force
g	Gravitational acceleration
h	Altitude (above ground level; AGL)
k_d	Damper proportionality constant
k_s	Spring proportionality constant
I_z	Moment of inertia about the yaw axis
l_m	Main wheels moment arm
l_r	Runway to centre of gravity length
l_s	Steering wheel moment arm
l_{sm}	Steering to main wheel moment arm
m	Mass
N	Yaw moment, north displacement or normal force
r	Yaw rate perturbation
R	Yaw rate, range or radius
R_{flare}	Flare range
R_{GP}	Glide path start range
S	Wing area
Y	Lateral force or Y-axis
U	Axial velocity
V	Lateral velocity
$\bar{V}$	Airspeed
W	Normal velocity or wind velocity component
X	Axial force or X-axis
Z	Normal force or Z-axis

Greek

α	Angle of attack, slip angle or angular acceleration
γ	Glide path angle
δ_a	Aileron perturbation from trim condition
δ_e	Elevator perturbation from trim condition
δ_r	Rudder perturbation from trim condition
δ_s	Steering wheel deflection angle
δ_t	Throttle perturbation from trim condition
μ_f	Rolling resistance coefficient
ρ	Air density
Ψ	Yaw angle

Subscript

app	Approach point variable
B_R	Runway body axis
c	Cornering
E	Inertial axis, east component or engine
f	Friction or finish
lm	Left main wheel
m	Main wheels
N	North component
rm	Right main wheel
s	Steering wheel, spring or start
W	Wind

1. Introduction

A large number of unmanned aerial systems (UAS) currently in service do not have the capability of performing autonomous take-offs and landings[1]. Instead, a human pilot is employed to handle these phases of the mission. This is usually done to mitigate risks and reduce the system complexity and cost. However, operational experience has shown that in many cases damage to an unmanned aerial vehicle (UAV) and its payload is due to human error during the take-off and landing phases of a mission[2]. Furthermore, to train a human pilot to a sufficient skill and experience

---

a, b Department of Electrical and Electronic Engineering,
Stellenbosch University,
Private Bag X1, Matieland, 7602, South Africa.
a Post-graduate Student
E-mail: jancor.roos@gmail.com
b Lecturer
E-mail: ikpeddle@sun.ac.za

level to handle UAV take-offs and landings, takes several years and a significant financial investment. A human pilot also imposes severe restrictions on the flight conditions under which a UAV can be operated; for example, a human pilot cannot land a UAV in thick fog or at night time.

Thus, although equipping a UAV with the ability to perform automatic take-off and landing increases the complexity of the system, it does have the potential of rendering a more versatile UAS while also potentially reducing the long term costs and risks involved in the take-off and landing phases of missions.

The first recorded automatic fixed-wing aircraft landing took place on August 23, 1937[3]. During the 1970's NASA developed control laws for steep glide slope tracking and flare manoeuvres[4], while the Boeing Corporation committed a fair amount of research to improve the automatic landing system used in their commercial airliners in the early 1980's[5]. In 1984 the Lockheed Corporations Skunk Works developed an autonomous take-off and landing system for the F-117A stealth fighter[6]. The system developed by the Lockheed Corporation proved very successful and was subsequently used in several United States Air Force attack aircraft[6]. Recent exponential growth in the use of UAVs and the UAS industry has stimulated widespread research into incorporating autonomous take-off and landing technologies into UAVs.

Motivated by the desire to develop an autonomous take-off and landing (ATOL) system, specifically for South African UAVs, the University of Stellenbosch's Centre of Expertise in Autonomous Systems conducted a two year research project on the subject. The test platform employed was a Reliance 0.46 size trainer model aircraft shown in figure 1. This aircraft had previously served as a platform for the successful development of a waypoint navigation autopilot described by Peddle and Milne[7]. With the basic in-flight control algorithms, avionics package and ground station in place, the objective of the ATOL research was to extend the autopilot to enable fully autonomous operation from take-off to landing.

To date, most miniature UAV autonomous landing research has been focused on rotary aircraft[8, 9], with fixed wing research typically focused on larger aircraft (60 kg and more) capable of carrying a wide range of advanced and accurate sensors[10-12]. The major restrictions imposed on the research presented in this paper were that the system should be lightweight (an all up mass of less than 5 kg), the cost should remain low and all autopilot computations should take place on-board the aircraft's two 8-bit fixed point microprocessors. The low cost constraint forced the use of only commercial-off-the-shelf (COTS) sensors in the problem solution. Autonomous take-off and landing research conducted on a similar class of UAVs can be found in Barber [8] and Montgomery[13]. However, in contrast to the research presented in this paper, Montgomery[13] made use of a specially develop four antenna GPS receiver and a full state estimator for autonomous control and landing, while Barber *et al.*[8] used optical flow sensors.

Hardware in the loop (HIL) simulation of the ATOL system is discussed, focusing specifically on the architecture of the HIL system and how the avionics package of Peddle and Milne[7] was extended to allow for HIL simulation. Flight test results are presented and compared to those predicted through HIL simulation. The practical results verify the success of the ATOL system and also correlate very well with the predicted simulation data. For further details of the research discussed see Roos[14] and Peddle[15].

Figure 1: The complete system

2. System Design

Several phases provide a system level solution to the ATOL problem for the case where only low cost, COTS sensors are used. More specifically, the sensors available during the research were limited to the following: a low cost GPS receiver (4 Hz update rate), absolute and differential pressure sensors, low cost micro-electrical-mechanical-systems (MEMS) angular rate gyroscopes and accelerometers and an ultrasonic altimeter.

2.1 Take-off sequence

A conventional runway take-off can be divided into three main phases. These are the ground run phase, the rotation phase and the climb out phase. During the ground run phase the aircraft is accelerated down the runway centre line until the velocity is high enough for the wing to generate enough lift to ensure safe lift-off. Once this predefined velocity is reached the aircraft is rotated to increase the angle of attack and therefore the lift generated by the wing to achieve lift-off. When the aircraft lifts off it enters the climb phase where it remains until a safe altitude is reached after which normal flight commences. At this point the take-off is considered complete. With these three main phases in mind, figure 2 defines the five take-off phases that constitute the take-off sequence used in this project. Phases 1 to 3 correspond to the ground run, phase 4 to rotation and phase 5 to climb out as described above.

The autonomous take-off sequence starts by placing the aircraft at the correct end of the runway for an upwind take-off with its nose aligned with the runway heading. The initial placement of the aircraft on the runway serves as the starting point for take-off and as shall be seen in the following section, as the aiming point for landing. Both the runway heading and the runway length are provided as parameters to the ATOL system. With the aircraft correctly positioned on the runway, the operator's duties are reduced to that of initiating the automatic take-off sequence.

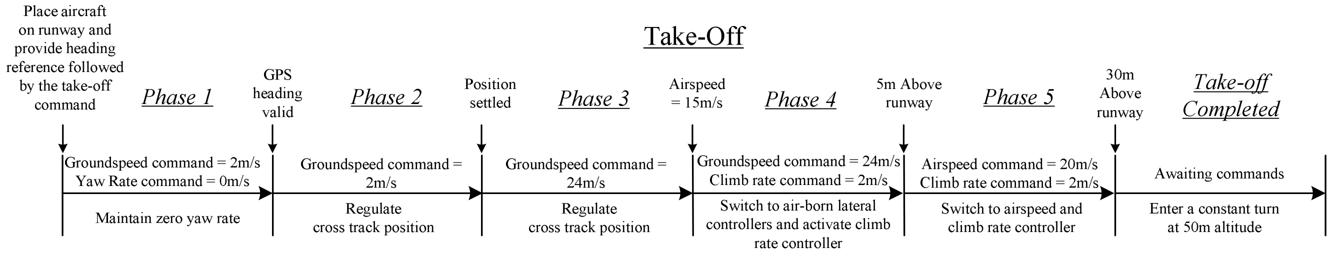

Figure 2: Take-off sequence

Of the sensors available, only the GPS is capable of providing low frequency lateral guidance information. However, while stationary the GPS ground heading information is erratic and the lateral actuation gains are zero. Phase 1 is thus introduced to move the aircraft out of this actuation and measurement singularity by commanding the ground speed magnitude to 2 m/s while regulating only the aircraft's yaw rate. This phase provides the opportunity for lateral position errors to accumulate thus promoting phase 2 of the take-off sequence. Here, valid GPS information is available and full lateral guidance is possible. With the ground speed regulated to 2 m/s, phase 2 continues until the cross track position relative to the runway centre line is within a certain acceptable bound.

The ground run of phase 3 is then executed where the aircraft is accelerated up to the take-off speed while regulating its cross track position relative to the runway centre line to zero. The rotation of phase 4 begins when the aircraft reaches its predefined take-off speed. Rotation is achieved by commanding a positive climb rate. Although other strategies that involve pitch angle regulation do exist they were expected to be less reliable given the quality of inertial sensors used. Lateral control is also switched to the yaw orientational control system of Peddle and Milne[7] at the start of phase 4. This simple rotation strategy proved to work well in simulation and in practice.

When an altitude of 5 m is reached phase 5 begins. Here the longitudinal control is handed over to the airspeed and climb rate controller of Peddle and Milne[7]. These controllers are used to conclude the climb out phase. For this project an altitude of 30 m was chosen as a safe altitude to consider the take-off sequence complete.

Finally, note that ground speed is used to control velocity on the runway. Although airspeed is a more important variable for take-off, it is difficult to measure accurately at low speeds because of the quadratic nature of differential pressure. Ground speed on the other hand can be obtained to a good degree of accuracy for take-off purposes by a GPS receiver. Although ground speed is controlled during the ground run phases, airspeed is used to schedule the rotation of phase 4 to avoid departure stalls.

2.2 Landing sequence

Conventional landing can equally be divided into three main phases. These are the approach phase, flare (touchdown) and roll-out phases. During the approach phase the aircraft is aligned with the runway and the airspeed is reduced while the altitude is gradually decreased as the glide path is flown. Usually at a predefined altitude the aircraft enters the flare phase in which the sink rate of the aircraft is decreased to allow for a safe and gentle touchdown on the runway with the airspeed just above the stall speed.

The roll-out phase is defined as the phase from the point of touchdown to where the aircraft comes to a standstill. At this point the landing is considered complete. With these three main phases in mind, figure 3 defines the seven landing phases that constitute the landing sequence used in this project. Phases 3 to 5 correspond to the approach, phase 6 to the flare and phase 7 to roll-out as described above.

When a landing command is issued by the system operator the landing sequence starts by entering phase 1 in which the aircraft is guided back to the runway by means of the conventional flight controllers developed in Peddle and Milne[7]. To minimise ground speed and thereby reduce the risk of damage to the aircraft at touchdown, it is desired to perform the landing sequence into the wind. To this end, an estimate of the wind direction is required. This estimate is obtained at the end of phase 1 by entering the aircraft into a constant turn and measuring the change in north and east displacement after a full circle is flown. The position change between the start and end points of the manoeuvre provides the direction of the constant wind vector as depicted in figure 4. By further measuring the time taken to fly the circle, the average wind magnitude can also be calculated. Note that by virtue of the measurement method, the effects of wind gusts are filtered over time thus providing an accurate constant wind estimate.

Based on the wind and runway heading information the system decides on the landing direction that ensures the largest head wind component. For the case where the desired landing direction is opposite to that of the take-off, the landing aiming point, which would otherwise coincide with the take-off initialisation point, is mirrored by the length of the runway.

With the inaccuracy of the GPS altitude measurement and the fact that ultrasonic altitude measurements are only reliably available below 5 m, barometric altitude was deemed the most suitable altitude feedback signal for the majority of the approach phase. Barometric altitude drift values, however, were found to be in the order of 4 m for typical flight times. Phase 2 is thus introduced to remove this drift for landing purposes. It involves executing a slow descent over the runway until valid ultrasonic returns are received. With the ultrasonic sensor accurate to within 1 cm, the barometric altitude offset can be removed and the landing sequence continued.

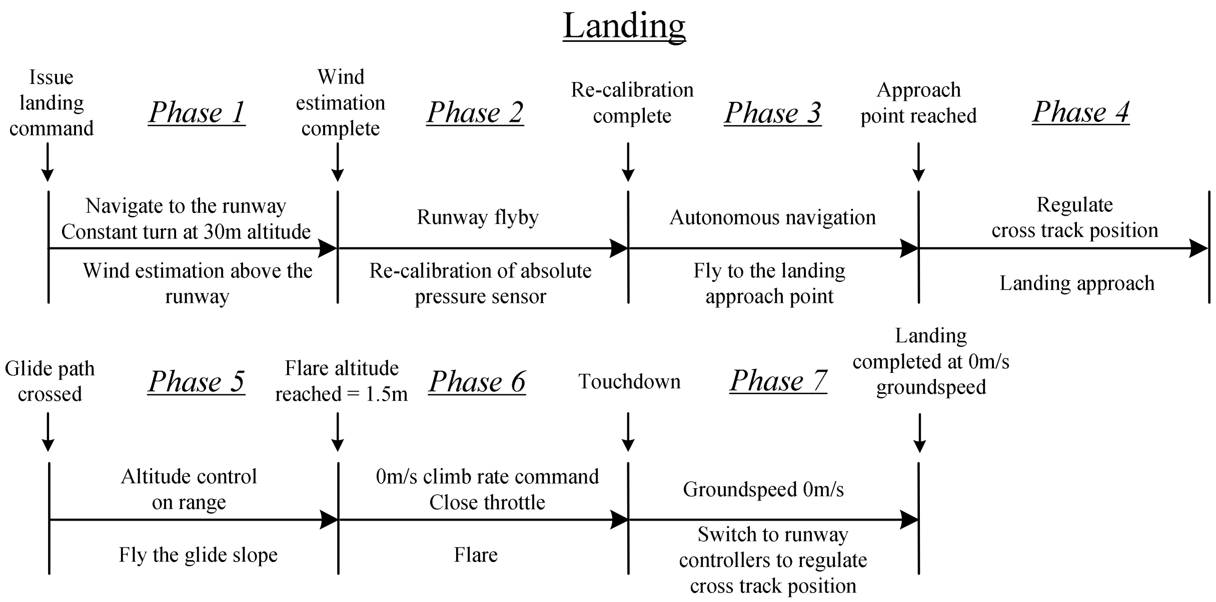

Figure 3: Landing sequence

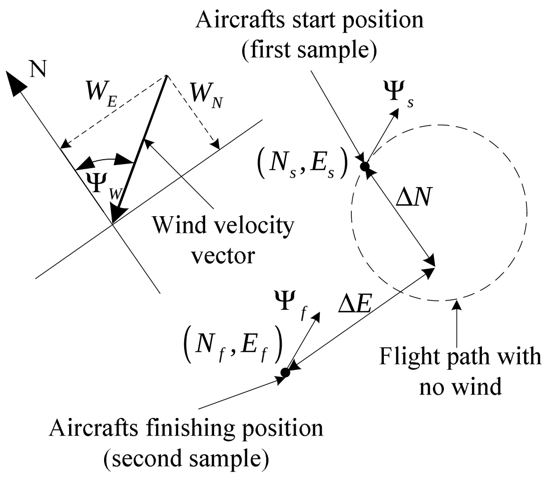

Figure 4: Wind estimation procedure

Phase 3 simply guides the aircraft to the approach point. Thereafter, phase 4 is entered where the aircraft is made to reduce airspeed and track the runway centreline before beginning the descent. This phase provides time for the aircraft's airspeed and lateral tracking to settle before beginning the critical descent phase. When the glide path is crossed the system enters phase 5. Tracking the glide path longitudinally involves regulating the altitude as a function of the range from the glide path origin (figure 5). Laterally, the cross track position relative to the runway centre line is constantly regulated using GPS information. A 6 ° glide slope was used in this project. When the aircraft's altitude decreases to below 5 m and valid ultrasonic returns are available, these measurements are used over barometric measurements for altitude tracking.

The ultrasonic sensor allows for precision altitude control during the final and most critical parts of the landing.

A number of methods exist to perform the flare manoeuvre of phase 6. In Blakelock[16], an exponentially decaying flight path is defined and when tracked results in a precision flare manoeuvre. Tracking complex flight paths can be computationally demanding and difficult to accomplish accurately with low cost sensors. A simpler flare approach was therefore adopted. This approach involves commanding the climb rate to zero and closing the throttle at a predefined altitude. The predefined altitude is based on the sink rate and the speed of response of the controller regulating climb rate. This simple strategy provided a practically feasible, computationally efficient solution to the flare problem. Furthermore, it also ensures that the aircraft flies the glide path for as long as possible and indirectly results in a positive pitch angle as the elevator attempts to regulate the climb rate to 0 m/s.

Just after touchdown the roll-out of phase 7 begins and lateral control is switched from the ailerons to the lateral ground controllers designed for take-off with the throttle closed. When the aircraft comes to a standstill the landing is considered complete.

3. Modelling

For control system design purposes, the aircraft can be considered a rigid body with aerodynamic, engine, gravitational and runway forces and moments acting upon it. Comprehensive models for the aerodynamic, engine and gravitational forces were developed by Peddle[15] for flight control design purposes. These models were used as a basis for the ATOL autopilot design. In addition to these models, a comprehensive runway model was developed to simulate the forces and moments that result due to the interaction of the aircraft's landing gear and the ground. The linear engine model of Peddle[15] was extended to a non-linear fixed pitch propeller piston engine model, where thrust is determined as a function of airspeed and throttle setting. A wind gust model was also developed through appropriate shaping of white noise. Wind gusts were modelled as they constitute the primary disturbance to the aircraft during take-off and landing.[14, 15]

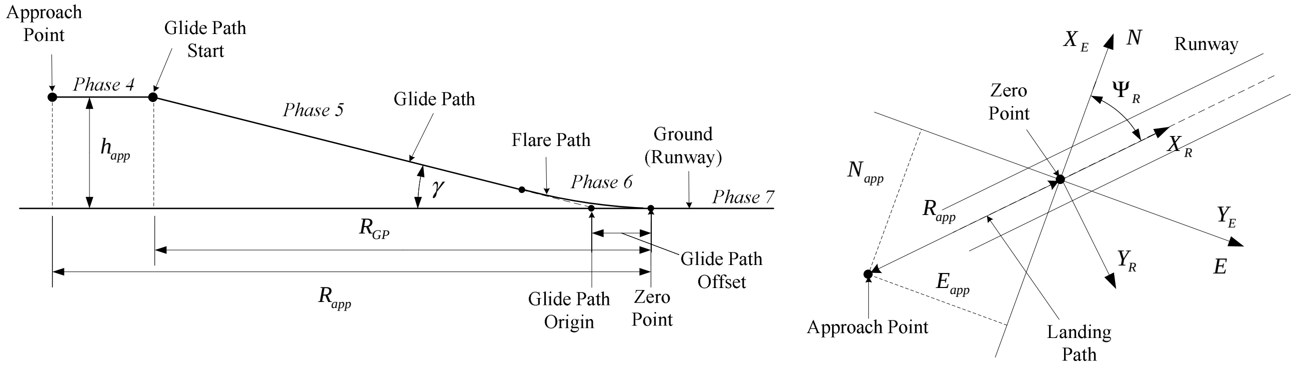

Figure 5: Landing path geometry (side and top view)

3.1 Non-linear runway model

This model is essential for simulating the take-off and landing process and for deriving the linearised models of subsection 3.2 for controller design purposes. The runway model was developed for a three wheeled aircraft with a tricycle undercarriage, but can easily be transformed to model a tail dragger. Development starts by defining the axis system used and then moves on to identify and discuss the main runway forces that act on the aircraft. A comprehensive normal force model was developed to model the dynamic weight transfer that occurs due to aerodynamic lift on the aircraft. This is especially important during take-off and landing where one wheel may touch down or lift-off before the others.

3.1.1 Axis system definition

The runway body axis system $F_{B_R} = \left(O_{B_R}, X_{B_R}, Y_{B_R}, Z_{B_R}\right)$ is defined as a right handed reference frame that is attached to the aircraft with its origin coinciding with the aircraft's centre of mass. The fundamental difference between the runway body axis system and a conventional body axis system is that the runway body axis system only yaws with the aircraft i.e. it does not roll and pitch. Thus, the runway body axis normal unit vector and the inertial axes normal unit vector are coincidental, making the runway body axis system a locally level axis system. All the forces discussed in the following section are referenced in the runway body axis frame.

3.1.2 Runway forces

According to Gillespie[17], frictional forces arise due to the axial friction between the wheel and the surface, the cornering forces act laterally relative to the wheel direction and arise due to slip angles on the wheel and normal forces arise due to the vertical reaction force of the ground on the wheels.

Friction force acting on a specific wheel was modelled as being directly proportional to the weight (normal force) on the wheel. Mathematically this relationship can be written as follows,

$$F_f = \mu_f N \tag{1}$$

where μ_f is the rolling resistance coefficient. Factors affecting the rolling resistance are[17]: tyre temperature, tyre inflation pressure, velocity, tyre material and design and tyre slip (defined later on). However, the influence of these factors was ignored as it is typically small and only complicates the modelling process. Thus, a fixed rolling resistance was used and calculated through experiment.

The slip angle α of a wheel is defined as the angle between the direction of travel and the direction of heading of the wheel. The cornering forces on a wheel are well modelled as being directly proportional to the slip angle α[17]. The proportionality constant, C_α is known as the cornering stiffness and is dependent on many variables of which normal load and inflation pressure are the most influential. Inflation pressure was assumed constant and the change in cornering stiffness with tyre load (normal force) was modelled as linear[17]. The cornering forces are thus modelled as follows,

$$\begin{aligned} F_c &= C_\alpha \alpha \\ &= C_{\alpha\alpha} N \alpha \end{aligned} \tag{2}$$

where N is the normal force at a specific tyre and $C_{\alpha\alpha}$ is the cornering coefficient of the tyre. It is important to note that at very low forward velocities, the slip angles can easily become large enough to violate the assumption that the cornering forces are linearly related to the slip angle. In this situation the model is no longer applicable. However, lateral control at very low velocities is not of great importance since lateral errors build very slowly. Thus, developing a more complex nonlinear lateral force model for low speeds is not warranted.

It is clear that the normal forces play an important role in the runway model with both the friction and cornering forces being directly proportional to the normal force at each wheel. To obtain the normal forces the aircraft's suspension was modelled by a spring-damper system at each wheel. With the vertical position and velocity of each suspension attachment point known, the corresponding spring and damper forces were summed to determine the local normal force for each wheel. A comprehensive description of the derivation of the normal force equations can be found in Roos[14].

3.1.3 Resultant forces and moments

Figure 6 shows a three-dimensional top, rear and side view suspension system. The subscripts *lm*, *rm* and *s* denote the left main, right main and steering wheels respectively and the subscript B_R denotes the runway body axis system. With the various runway forces acting on each wheel

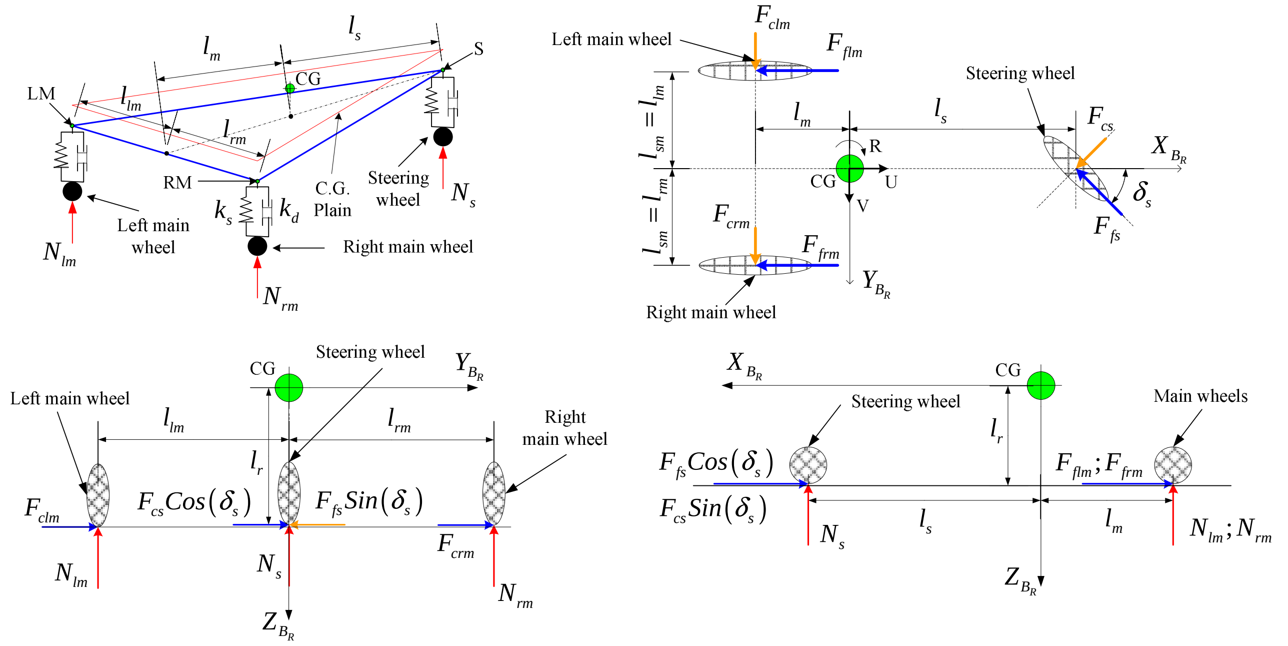

Figure 6: Runway force diagrams

identified and modelled, the resultant forces and moments acting on the aircraft can be written as follows,

$$\sum F_x = -F_{flm} - F_{cs}Sin(\delta_s) - F_{fs}Cos(\delta_s) - F_{frm} = F_{x_{B_R}} \tag{3}$$

$$\sum F_y = F_{clm} + F_{cs}Cos(\delta_s) - F_{fs}Sin(\delta_s) + F_{crm} = F_{y_{B_R}} \tag{4}$$

$$\sum F_z = -N_s - N_{rm} - N_{lm} = F_{z_{B_R}} \tag{5}$$

$$\begin{aligned}\sum L_{cg} &= -F_{clm}l_r + N_{lm}l_{sm} - F_{cs}Cos(\delta_s)l_r + \\ &F_{fs}Sin(\delta_s)l_r - F_{crm}l_r - N_{rm}l_{sm} = L_{B_R}\end{aligned} \tag{6}$$

$$\sum M_{cg} = N_s l_s - N_{lm}l_m - F_{cs}Sin(\delta_s)l_r - N_{rm}l_m = M_{B_R} \tag{7}$$

$$\begin{aligned}\sum N_{cg} &= F_{cs}Cos(\delta_s)l_s - F_{clm}l_m - F_{flm}l_{sm} \\ &-F_{fs}Sin(\delta_s)l_s - F_{crm}l_m + F_{frm}l_{sm} = N_{B_R}\end{aligned} \tag{8}$$

3.2 Linear runway model

The following assumptions were made to simplify the full non-linear runway model:

- The steering angle δ_s is small ($-10^\circ \le \delta_s \le 10^\circ$).
- The roll and pitch angles (Φ and Θ) are zero on the runway.
- Only the steering wheel and the rudder-fin combination contribute to the yaw moment acting on the aircraft while it is on the runway. All other aerodynamic, engine and runway effects that contribute to the yaw moment are ignored.
- The lateral velocity on the runway (v) is negligible and the ratio R/U is small.

Combining the runway force and moment equations given by equation 3 and with the respective aerodynamic, engine and gravitational force and moment equations from Peddle and Milne[7], and then applying the assumptions above, yields the axial and yaw rotational dynamics in a simplified form below,

$$\delta_t - \mu_f \cdot mg + \frac{1}{2}\rho S\left(\mu_f C_L - C_D\right)\bar{V}^2 = m\dot{U} \tag{9}$$

$$\left[\frac{l_m l_s}{(l_s + l_m)}C_{\alpha\alpha}\left(mg - \frac{1}{2}\rho\bar{V}^2 SC_L\right)\right]\delta_s + \left[\frac{1}{2}\rho\bar{V}^2 S_F l_F \frac{\partial C_{L_F}}{\partial \delta_r}\right]\delta_r = I_z\dot{r} \tag{10}$$

Linearisation of the longitudinal dynamics of equation 9 was achieved by simply ignoring the friction force terms (typically small) together with the aircraft's drag. These terms are instead considered disturbances to the axial dynamics and it is left as the task of the control system to reject their effects. Consequently, the design of the axial acceleration controller in section 4.3 is influenced to cater for these now un-modelled disturbances.

Successive linearisation was chosen as the method with which to handle the airspeed non-linearity in the lateral dynamics of equation 10. In turn this allowed for a gain scheduling control law to be employed. Although feedback linearisation[18] (static inversion in this case) could have been used to provide a continuous inversion of the nonlinearities in equation 10, practical implementation restrictions forced the use of a successive linearisation/gain scheduling approach. This was due to the fact that it was more computationally efficient to implement a gain scheduling controller on an 8-bit fixed point microcontroller.

4. Control System Design

4.1 Control system overview

Figure 7 shows a block diagram representation of the autopilot after the controllers required for take-off and landing were added to the navigating autopilot block diagram of Peddle and Milne[7]. Fully shaded blocks represent the controller's added for take-off and landing while partially shaded blocks were used during both conventional flight and take-off and landing.

The general strategy adopted during the design of the control system was that of output feedback successive loop closure. Using output feedback negated any need for estimators to be designed which in turn placed less of a burden on the 8 bit on-board microprocessors. Successive loop closure was adopted for a number of reasons. Firstly, it provides a very intuitive approach to the control system design. It results in very simple control structures that although may not be optimal in some sense, can easily be practically fine tuned. Furthermore, robustness measures such as gain and phase margins can be directly used to provide the designer with an intuitive feel of the system's sensitivity to uncertainty. Finally, successive loop closure also simplifies any gain scheduling required since only the inner most aircraft dependent loops need to be scheduled while outer kinematic loops tend to have fixed feedback gains.

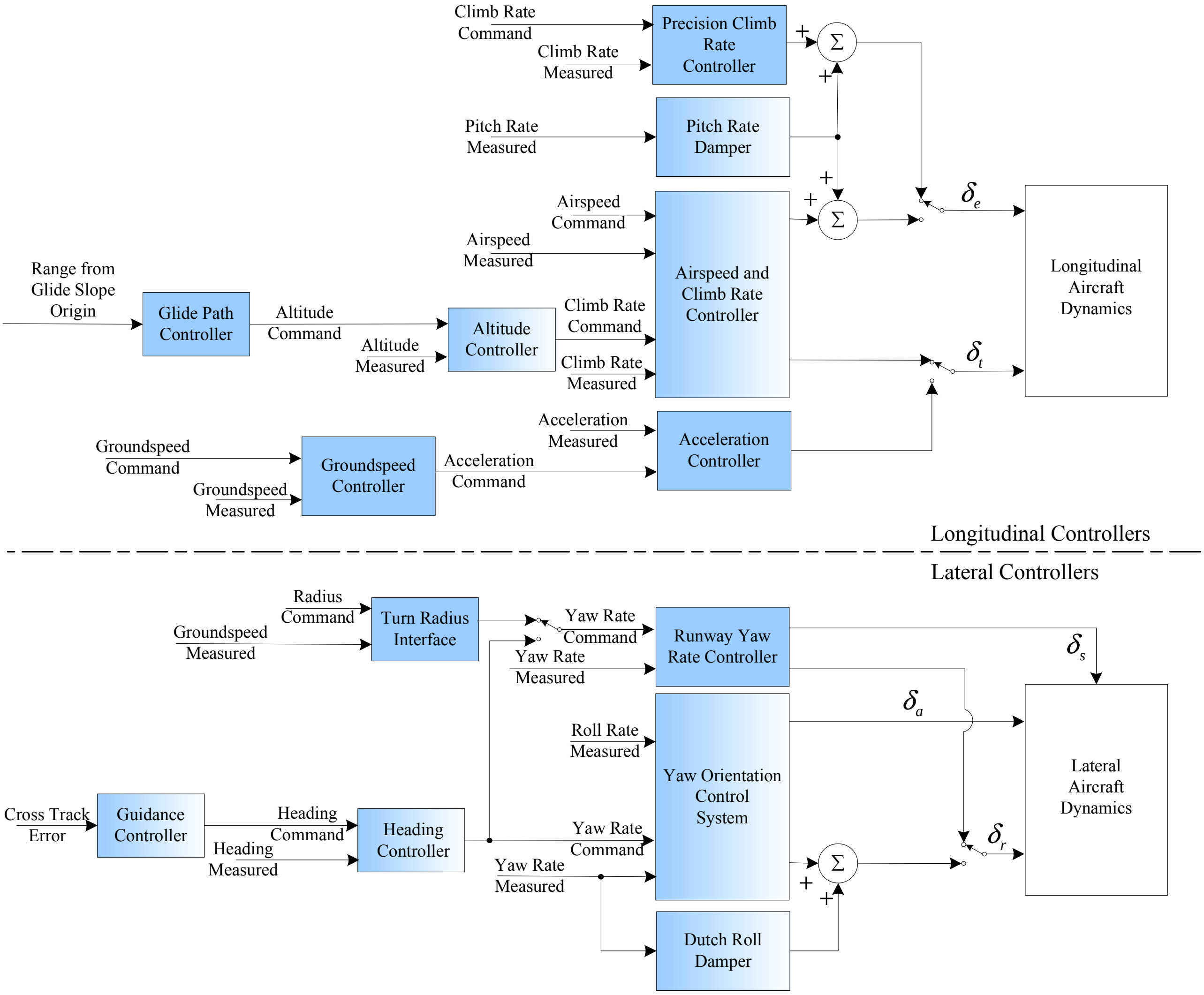

Figure 7: Autopilot block diagram

4.2 Extension of conventional flight controllers

The design of the controllers required for conventional straight and level flight is well documented in Peddle and, Milne[7] and Peddle[15]. However, these controllers were designed for a single operating airspeed and were found to yield unacceptable performance at the lower airspeeds. Gain scheduling of the inner air speeds and climb rate controller as well as the yaw rate controller of figure 7 was used to extend the air speed operating range of these controllers. The outer guidance controller of figure 7 also required gain scheduling because of the dependency of the cross track error closure rate on velocity.

4.3 Controllers added for take-off and landing

4.3.1 Axial acceleration and groundspeed controllers

Longitudinal groundspeed control through phases 1 to 4 of the take-off sequence (figure 2) was achieved by first feeding back the axial acceleration error to the throttle actuator. This inner loop was added to provide lead compensation for the outer ground speed control loop since the GPS ground speed measurement is only updated at 4 Hz and has a single cycle delay. The inner acceleration control loop also allowed for faster disturbance rejection of un-modelled axial disturbances such as those from wheel friction, drag and wind gusts.

The acceleration controller architecture is of a proportional-integral (PI) nature to compensate for the uncertain steady state gain from throttle to axial acceleration as well as biases in the throttle actuation system. A high phase margin was designed for to ensure robustness to system uncertainties. The upper bandwidth of the control loop is limited by noise on the acceleration feedback signal, the bandwidth of the thrust actuator and the absence of an active breaking system.

With this inner controller in place, an outer ground speed controller was designed by feeding the ground speed error back to form an axial acceleration command. A direct digital design was performed allowing the single cycle delay to be compensated for.

4.3.2 Precision climb rate controller

A precision climb rate controller was designed to cater for the rotation and flare phases of the take-off and landing sequences. This controller involves feedback of the climb rate signal to the elevator only. Although the throttle does influence the climb rate, its effect was not included in the design of the controller. This simplification is justified by the fact that the controller would only operate when the throttle is either fully closed (while flaring) or largely open (under control of the groundspeed controller during rotation and climb out).

The design of a separate precision climb rate controller for specific parts of the take-off and landing was motivated by the desire to obtain a fast, precise climb rate response for the rotation and flare phases of flight. The controller design is of a PI nature which provided the necessary design freedom for good steady state tracking and appropriate regulation of the dynamic response. The bandwidth of the controller is limited by the noise on the climb rate signal.

4.3.3 Runway yaw rate controller

From equation 10, it is clear that the dominant actuator for yaw rate control on the runway depends on the airspeed. To simplify the control system design, this multiple input system was reduced to a single input system by enforcing a 2:1 relationship between the steering wheel and rudder commands. Although seemingly arbitrary, this relationship was motivated by practical insight from the human safety pilot.

Single-Input-Single-Output (SISO) design techniques were used with gain scheduling to design the yaw rate controller. The controller was designed for maximum wind gust disturbance rejection by increasing the bandwidth as far as possible with the upper bound enforced by the susceptibility of the controller to the high frequency noise present on the low cost gyroscopes. Furthermore, an integral term was introduced into the compensator to negate the effects of aircraft asymmetry (particularly on the nose wheel), to reject any constant cross wind disturbances and to counter propeller torque and helical slipstream effects.

4.3.4 Runway heading and guidance controllers

Lateral guidance during phases 1 to 3 of the take-off sequence (figure 2) and after touchdown in the landing sequence (figure 3) was achieved by regulating the cross track error from the runway centre line. Guidance control was achieved in a successive loop closure fashion with the heading controller driving the yaw rate controller of the previous subsection and the guidance (cross track position) controller driving the heading controller. Heading and position measurements were obtained from a 4 Hz single cycle delay GPS receiver. For this reason both controllers were designed directly in the discrete time domain. Both controllers involved only simple proportional feedback loops with the majority of the disturbance and uncertainty rejection handled by the inner yaw rate control system. Finally, the guidance controller was also gain scheduled with velocity due to the dependency of the cross track error rate of closure on velocity.

4.3.5 Glide path controller

The standard in air altitude controller of Peddle and Milne[7] was used to fly the glide slope during phase 5 of the landing sequence by providing altitude commands based on range from the glide path origin. To avoid the steady state altitude error required to maintain the constant sink rate associated with the glide slope, the necessary sink rate was fed forward to the climb rate controller. This allowed for closed loop glide slope control without the need for extra controllers.

5. Avionics and Hardware in the Loop Simulation

In this section, the low cost avionics package used to implement the control algorithms of the previous section is described. The avionics package is an extension of the one developed for waypoint navigation in Peddle and Milne[7]. The avionics was primarily extended to allow for hardware in the loop simulation – an essential feature to minimise flight test risks. A brief overview of the architecture of the hardware in the loop simulator is also provided.

5.1 Low cost avionics package

Figure 8 shows a block diagrams of the avionics package onboard the aircraft and the ground station. Shaded blocks represent newly added hardware or functionality while partially shaded blocks indicate modifications to the original avionics package. The most significant modification to the avionics is the addition of the HIL interface which allows the avionics package to use either its own onboard sensor signals or those from an external source. A signal multiplexing scheme at the analogue to digital converter level was used to implement the HIL interface. Practical autonomous take-off and landing was accomplished using only the low cost sensors available in the avionics package. These sensors included MEMS angular rate gyroscopes, MEMS accelerometers, differential and absolute pressure sensors, a low cost GPS receiver and an ultrasonic range finder. All computation occurred onboard the aircraft using two fixed point, 8-bit Reduced Instruction Set Computer (RISC) architecture microprocessors and the total avionics consumed less than 5 W.

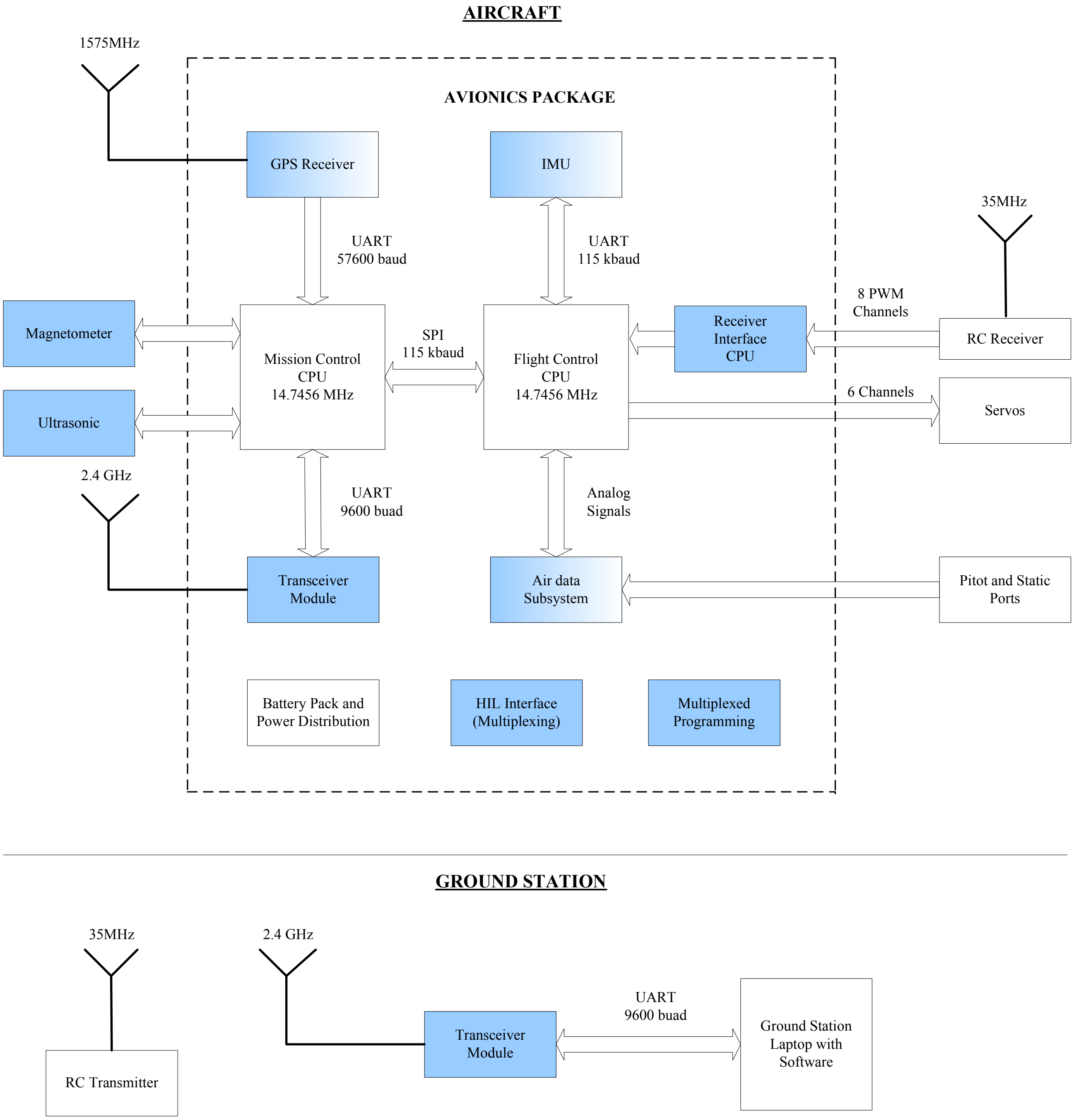

Figure 8: Aircraft and ground station block diagram

5.2 Hardware in the loop simulator

In order to thoroughly test the control algorithms implemented on the avionics package, a hardware in the loop simulator was developed[19]. A functional block diagram of the HIL simulator is shown in figure 9. The HIL system was designed to operate from MATLAB's Simulink environment with a custom three-dimensional graphics display for visualisation purposes. A HIL simulator distribution board was designed to act as the interface between the avionics package and the simulator computer. The flow of data is clearly seen from figure 9.

The HIL simulation was essential to instil a high degree of confidence in the control algorithms and it supported the cost constraints of the research by reducing the risk associated with potentially expensive flight tests. The HIL simulator was also used to quantify effects such as sensor noise, microprocessor quantisation, wind, actuator delay and saturation, longitudinal and lateral coupling and the severity of linearisation assumptions. For a more detailed discussion on the HIL simulator design refer to Hough[19].

6. Autonomous Take-Off and Landing

With the ATOL control system designed, a number of flight tests were held to practically verify the autopilot. The results verify the practical success of the ATOL control algorithms. In total, the aircraft successfully performed 5 autonomous take-offs and 3 autonomous landings, the difference in number being attributed to the fact that the autopilot did not always land the aircraft when the take-off controllers were being tested.

In subsection 6.1, data from the runway controllers that could be explicitly tested outside of an entire take-off or landing sequence is presented. Then in subsections 6.2 and 6.3, data from a take-off and landing sequence respectively is presented. All practical data presented was recorded from the on-board sensors and thus includes sensor noise.

Figure 11 shows the response of the runway heading controller together with the simulated response to an 80º step in heading. The associated yaw rate during this manoeuvre is also shown. With the accurate yaw rate response discussed previously, this level of correlation between the practical and simulated results was expected due to the successive loop closure controller architecture employed.

Figure 12 shows the lateral response during autonomous taxing with the runway (8 m wide), centre line and direction of travel superimposed. The guidance controller is seen to perform very well with the runway centre line being tracked to a good degree of accuracy. The small offset is most likely due to a bias on the yaw rate gyroscope since there are no integrators in the outer guidance loops. With the inner yaw rate and heading controllers functioning well, this accuracy of response was expected due to the controller architecture.

Figure 13 shows the longitudinal responses (groundspeed and acceleration controller response), during autonomous taxing. With a 3 m/s ground speed command issued, some differences between the practical and simulated responses can be seen. These differences can be

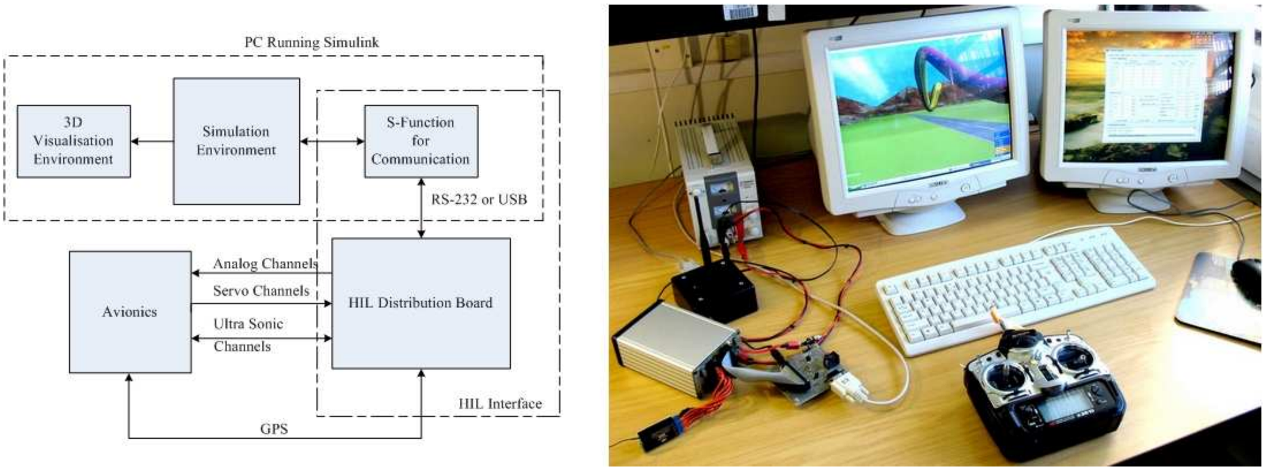

Figure 9: HILS functional block diagram

6.1 Runway controllers

Figures 10 to 13 show the responses of the individual controllers designed for use on the runway. Figure 10 shows the practical response of the runway yaw rate controller to a 30 °/s step command in yaw rate, together with the theoretical response from the HIL simulator. The actual and theoretical yaw rate responses correspond very well. The correlation verifies the accuracy of the runway model and validates the linearization assumptions made in section 3.2.

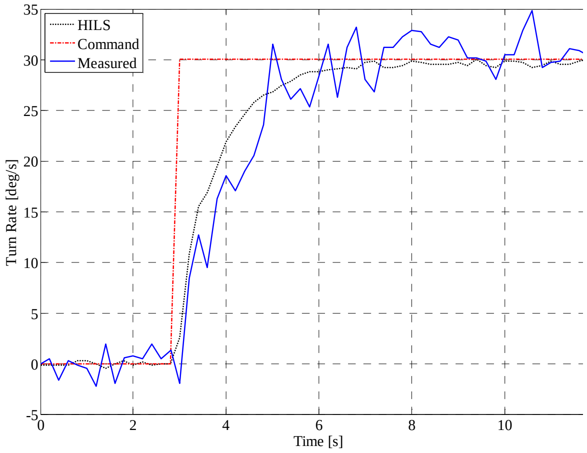

Figure 10: Runway yaw rate controller response

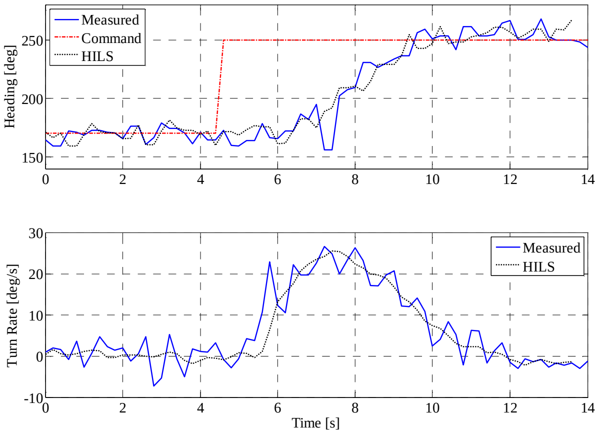

Figure 11: Runway heading controller response

attributed to several sources of which the most influential are errors in the engine model used for design and the effects of ignoring the friction forces in the longitudinal linearisation process. The small steady state groundspeed error is most likely due to misalignment of the axial accelerometer and the absence of an integral term in the outer groundspeed controller. The initial 2 seconds of delay in the simulated response is due to the expected actuator dead band that was incorporated into the non-linear engine simulation model.

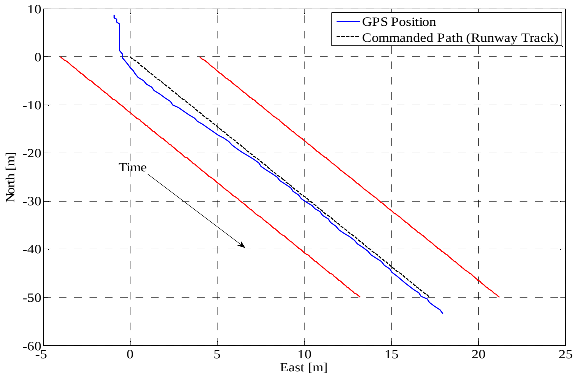

Figure 12: Runway guidance controller response

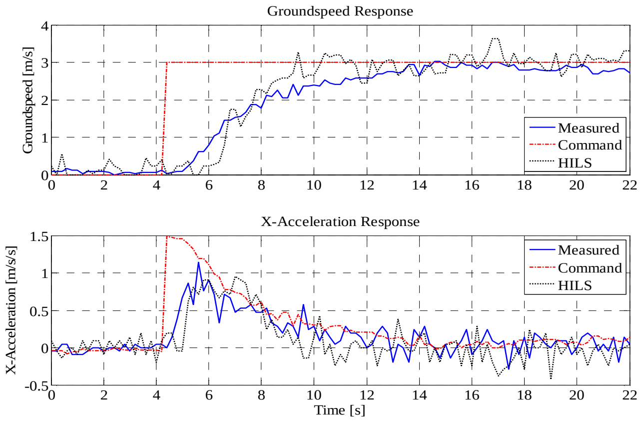

Figure 13: Axial Acceleration and Ground Speed Controller Response

6.2 Take-off

Figures 14 to 16 show the practical results obtained from performing the take-off sequence of figure 2. The initial 7 seconds is used for phases 1 and 2 to obtain a valid GPS heading measurement and to re-align the aircraft with the runway centre line before the take-off run starts in phase 3. Note the sharp increase in the airspeed measurement just as phase 3 is entered. This increase is caused by airflow from the propeller coupling into the pitot tube as the throttle is opened for the ground roll. The coupling can also be seen in phase 5 were the airspeed is controlled to 20 m/s while the ground speed measurement is only 15 m/s. Mounting the pitot tube in the wing instead of above the propeller as was done in this project (shown in figure 1) could prevent this coupling.

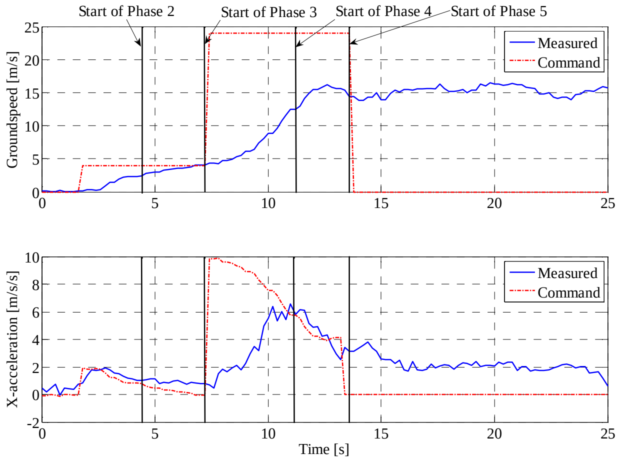

Figure 14: Take-off results

The climb rate measurement in figure 15 shows excessive overshoot during rotation and the initial moments of climb out in phases 4 and 5. The overshoot is most likely due to modelling errors in the elevator effectiveness, with the elevator being more effective in practice than in simulation.

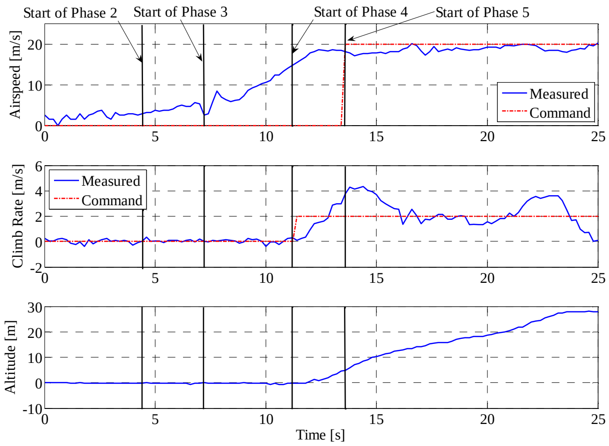

Figure 15: Take-off results

Figure 16 shows the two dimensional GPS position of the aircraft during take-off with the runway limits for a 6m wide runway superimposed.

It can be seen that the aircraft yaws slightly to the right during take-off. This was due to the crosswind present during the flight test. As the aircraft gains speed the steering wheel looses effectiveness making the aircraft susceptible to crosswind disturbances. However, the integral nature of the yaw rate controller would ultimately drive it back to zero if given the time. A similar crosswind effect was also seen during HIL simulation and was deemed acceptable for practical purposes. Finally, note how the lateral controllers used for conventional flight pull the aircraft back onto the runway centre line as it continues to climb. Fourteen seconds after rotation an altitude of 30 m is reached signalling the end of the take-off sequence.

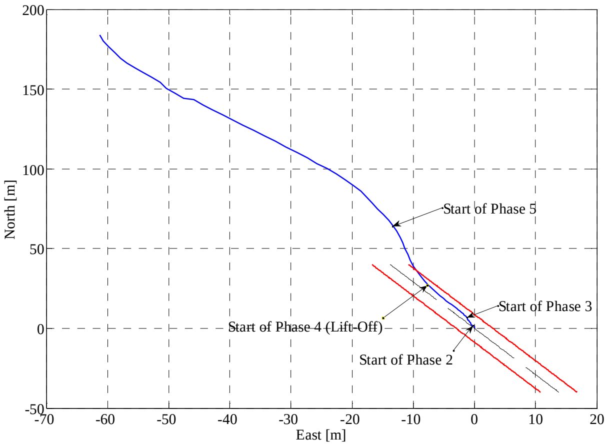

Figure 16: Take-off results

6.3 Landing

Figure 17 to figure 19 show the reference commands and system responses while executing the landing sequence of figure 3. The first two phases of the landing sequence were not executed as part of the presented landing sequence.

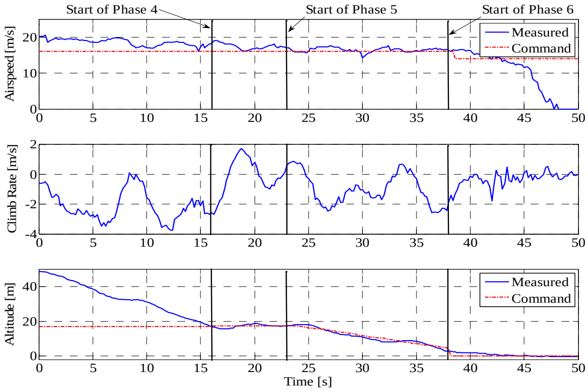

Figure 17: Landing results

Both phases were however practically tested and verified during a separate flight test. The presented flight data therefore starts at phase 3 during the final moments of navigation towards the approach point and all timelines in figure 17 to figure 19 continue relative to this point.

From figure 17, note the slight airspeed oscillation as the aircraft tracks down to the desired airspeed of 16 m/s. The oscillation is caused by the airflow from the propeller coupling into the pitot tube and the large feedback gain from airspeed error through to throttle. However, despite this lightly damped oscillation, the aircraft tracks to the desired airspeed adequately. Figure 18 shows that throughout the landing sequence the altitude reference is tracked with acceptable precision, never deviating more than 2 m from the reference command (note that the ultra sonic altitude shown is only valid below 5 m). However, the altitude response also displays periodic motion. The oscillation is again most likely caused by the pitot tube system coupling with the propeller and the fact that airspeed and climb rate are controlled with a MIMO controller.

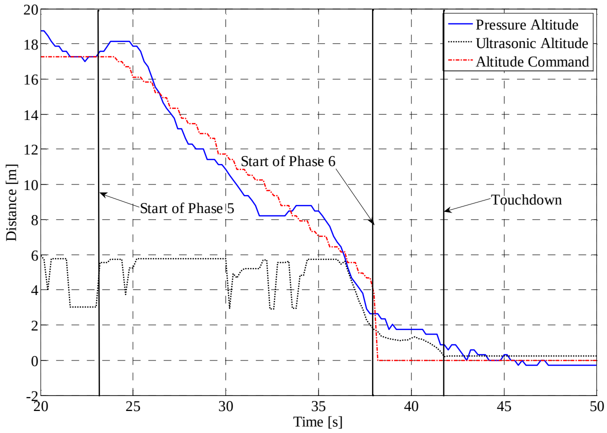

Figure 18: Landing results

The flare of phase 6 was initiated at 38.4 s. The precision climb rate controller response was faster than expected, causing the aircraft to flare more sharply and hold an altitude of 1 m. Since the throttle was closed the aircraft glided the final meter and touchdown (the start of phase 7) occurred at 42 s. The sharp flare can again be contributed to modelling errors in elevator effectiveness as was seen during the take-off rotation phase.

From the lateral response shown in figure 19, the cross track error on approach is seen to settle faster than expected. The approach point can therefore be moved closer to the runway with the lower limit enforced by the time required for the airspeed to decrease during phase 4. Upon touchdown, note how the runway guidance controller pulls the aircraft back onto the runway as desired. At 48 s the aircraft comes to a standstill, concluding the landing sequence.

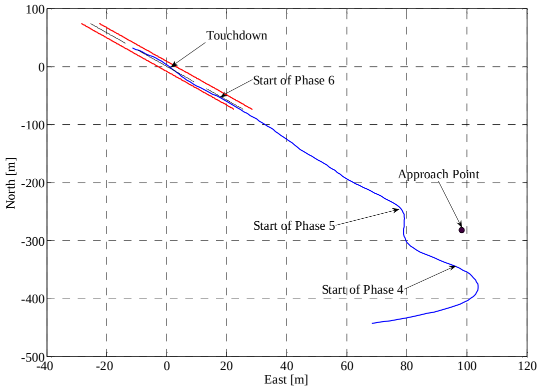

Figure 19: Landing results

Finally, note that with the current controller architecture, the steady state lateral cross track error can be up to 10 m for a worst case gyroscope bias and GPS drift error. This translates into a minimum required runway width of 20 m for a guaranteed landing. However practical flight test results show that an 8 m wide runway is acceptable for almost all cases. Of course, the minimum runway width could be greatly decreased with the use of a better absolute positioning sensor.

7. Conclusion

The practical success of the autopilot can largely be attributed to the simple, practical control strategies employed and the many hours of HIL simulation conducted. When combined with the in flight controllers of Peddle and Milne[7], the ATOL control algorithms make fully autonomous flight from take-off to landing of the UAV in figure 1 possible.

One of the major challenges currently facing the autonomous landing of miniature UAVs is the availability of an accurate, low cost, light, atmospheric change independent, height above ground (HAG) sensor with a measurement range of at least 20 m. Such a sensor would allow awkward phases such as phase 2 of the landing sequence to be removed and allow for safe landings after long periods of flight (where barometric pressure may have drifted substantially.[8] Furthermore, accurate altitude measurements can be used to obtain more accurate climb rate signals which in turn would allow for more precise control during the crucial flare and rotation phases of take-off and landing.

Future research will involve investigating an immediate, low cost substitute for an improved climb rate signal. This will involve combining the barometric climb rate with the ultrasonic altitude in a stochastically optimal sense for use in the rotation and flare phases of flight. Inclusion of an optical flow sensor[8] to improve state estimation will also be considered, subjected to the cost and computational constraints of the system. With the ever decreasing price of digital processing power, incorporating fast, floating point processors in low cost automation solutions is becoming more and more feasible. This opens up opportunities for implementing more complex control and estimation solutions to problems such as ATOL. Instead of using output feedback as was done in this project, Kalman filters can be used to optimally combine all low cost sensors to provide better feedback signals. Floating point processing also allows for techniques such as feedback linearisation to be practically implemented for dynamic range extension purposes. Although these techniques will be investigated, it is important to remain aware of the increased interdependency they introduce to a control system. Thus, a balance needs to be found between performance and practical risk of failure for a robust, low cost ATOL solution.

8. Acknowledgements

The authors would like to thank Denel Dynamics and the National Research Foundation's THRIP program for funding the project. The Helderberg Radio Flyers club is acknowledged for allowing the use of their facilities for flight tests. The steady hands of our safety pilot, Dr. Kas Hamman, were greatly appreciated during the flight tests.

References

1. *Schawe D, Rohardt CH and Wichmann G*, Aerodynamic design assessment of Strato 2C and its potential for unmanned high altitude airborne platforms, *Aerospace Science and Technology*, 2002, 6.
2. *Attar M, Wahnon E and Chaimovitz D*, Advanced Flight Control Technologies for UAVs *2nd AIAA Unmanned Unlimited Conference and Workshop and Exhibit*, San Diego, CA. 15-18 September 2003.
3. *Sprinkle J, Eklund JM and Sastry SS*, Deciding to land a UAV safely in real time, *American Control Conference*, Portland, OR, USA, June 2005, 5 3506-3511.
4. *Halyo N*, Development of a Digital Automatic Control Law for Steep Glide Slope Capture and Flare, NASA Report No. CR-2834, prepared by University of Virginia, June 1977.
5. *Lambregts AA*, Avoiding the Pitfalls in Automatic Landing Control System Design, A82-39013, Boeing Commercial Airplane Company, 1982.
6. *Rich BR and Janos L*, Skunk Works, Back Bay Books / Little Brown and Company, 1994.
7. *Peddle IK and Milne GW*, Development of a low cost waypoint navigation autopilot for an unmanned aerial vehicle, *R&D Journal of the SAIMechE*, 2007, 23(2), 18-24.
8. *Barber DB, Griffiths SR, McLain TW and Beard RW*, Autonomous landing of miniature aerial vehicles, *AIAA Infotech@Aerospace*, No. 2005-6949, 2005.
9. *Shang J and Shi Z*, Vision-based runway recognition for uav autonomous landing, *International Journal of Computer Science and Network Security*, 2007, 7(3) 112-117.
10. *Accardo D, Esposito F, Cimmino G, Moccia A, Ciniglio U and Corraro F*, Integration of advanced altimetric systems for UAV vertical navigation during landing manoeuvre, 3rd AIAA *Unmanned Unlimited Technical Conference, Workshop and Exhibit*, No. AIAA 2004-6318, Chicago, Illinois, September 2004.
11. *Gutt GM, Fischer SL, Sheen JH, Lawrence DG and White SN*, Precision autoland guidance of the X-31 aircraft using IBLS – The integrity beacon landing system, *AIAA Guidance, Navigation, and Control Conference and Exhibit*, Providence, Rhode Island, August 2004.
12. *Riseborough P*, Automatic Take-Off and Landing Control for Small UAV's, BAE SYSTEMS, Melbourne, Australia, 2004.
13 *Montgomery PY*, Carrier Differential GPS as a Sensor of Automatic Control. PhD thesis, Department of Aeronautics and Astronautics, Stanford University. 1996.
14. *Roos JC*, Autonomous Take-Off and Landing of a Fixed Wing Unmanned Aerial Vehicle, MScEng thesis, Department of Electrical and Electronic Engineering, Stellenbosch University, 2007.
15. *Peddle IK*, Autonomous Flight of a Model Aircraft, MSc Eng thesis, Department of Electrical and Electronic Engineering, Stellenbosch University, 2005.
16. *Blakelock JH*, Automatic Control of Aircraft and Missiles. 2nd ed. New York: Wiley-Interscience, 1991.
17. *Gillespie TD*, Fundamentals of Vehicle Dynamics. Warrendale: Society of Automotive Engineers, 1992.
18. *Slotine JJ and Li W*, Applied Non-linear Control, New Jersey, Prentice Hall, 1990.
19. *Hough WJ*, Autonomous Aerobatic Flight of an Unmanned Arial Vehicle, MScEng thesis, Department of Electrical and Electronic Engineering, Stellenbosch University. 2006.